Geophysical Research Letters

RESEARCH LETTER
10.1029/2021GL093541

Key Points:

- We present the first simultaneous observation of L-band Synthetic Aperture Radar (SAR) scintillation stripes and 630-nm airglow depletion in northern Brazil
- The results show that plasma density irregularities in equatorial plasma bubbles are the source of observed SAR scintillation
- SAR data show the occurrence of scintillation stripes and plasma density gradients near airglow depletion region

Supporting Information:

Supporting Information may be found in the online version of this article.

Correspondence to:

H. Sato,
hiroatsu.sato@dlr.de

Citation:

Sato, H., Kim, J. S., Otsuka, Y., Wrasse, C. M., Rodrigues de Paula, E., & Rodrigues de Souza, J. (2021). L-band Synthetic Aperture Radar observation of ionospheric density irregularities at equatorial plasma depletion region. *Geophysical Research Letters*, *48*, e2021GL093541. https://doi.org/10.1029/2021GL093541

Received 30 MAR 2021
Accepted 10 AUG 2021

L-Band Synthetic Aperture Radar Observation of Ionospheric Density Irregularities at Equatorial Plasma Depletion Region

Hiroatsu Sato[1], Jun Su Kim[2], Yuichi Otsuka[3], Cristiano Max Wrasse[4], Eurico Rodrigues de Paula[4], and Jonas Rodrigues de Souza[4]

[1]German Aerospace Center (DLR), Institute for Solar-Terrestrial Physics, Neustrelitz, Germany, [2]German Aerospace Center (DLR), Microwaves and Radar Institute, Wessling, Germany, [3]Institute for Space-Earth Environmental Research (ISEE), Nagoya University, Nagoya, Japan, [4]National Institute for Space Research (INPE), São José dos Campos, Brazil

Abstract Plasma density irregularities in the equatorial ionosphere are thought to cause the distortions of L-band Synthetic Aperture Radar (SAR) images, which have been observed in recent years, but the origin of the image distortion has not yet been clearly identified experimentally. We report on the first simultaneous observation of equatorial plasma bubbles (EPBs) by the ALOS-2/PALSAR-2 satellite and ground 630-nm airglow imager in northern Brazil. We observe stripe-like distortions of SAR signal power that are aligned in the direction of local magnetic field lines. The stripe-like patterns are observed in the vicinity of airglow depletion. The result shows that the observed L-band SAR stripes are caused by ionospheric scintillation due to plasma irregularities with the scale size of hundreds of meters associated with EPBs. We show that the SAR scintillation stripes are predominantly found at the location of sharp density gradients in the two-dimensional form.

Plain Language Summary Plasma density irregularities in Earth's ionosphere scatter various radio waves. Such density irregularities are known to exist at large-scale density depletion structures known as equatorial plasma bubbles. Plasma bubbles occur at night-time in low latitude regions. We observed plasma bubbles by using a radar satellite and ground optical imager. The results demonstrate that two-dimensional structure of density irregularities of plasma bubble can be extracted when the density irregularities imprint stripe-like patterns on the radar image. This study suggests that the radar image can be a useful tool to observe Earth's ionosphere.

1. Introduction

Plasma density depletions in the post-sunset equatorial ionosphere, known as Equatorial Plasma Bubbles (EPBs), are thought to be a primary source of plasma irregularities on a scale from centimeters to kilometers that scatter radio waves at various wavelengths (e.g., Basu et al., 1978; McNamara et al., 2013; Saito et al., 2008; Tsunoda, 1980). As the low-density plasma in the bottom side of the F region transports into the topside F-region with the thrust from Rayleigh-Taylor instability, smaller density irregularities can be generated by secondary instability processes inside EPBs (Yokoyama et al., 2014).

Two-dimensional large-scale structures of the density depletion along the magnetic field lines have been studied by using 630-nm airglow imaging and GPS total electron content (TEC) mapping techniques (e.g., Otsuka et al., 2002; Takahashi et al., 2015). While plasma irregularities at low latitudes have been well studied by means of GPS scintillation (e.g.,Kintner et al., 2007), a two-dimensional observation of scintillation sources for L-band radio signals that are comparable to the horizontal structure of the density depletion is not yet available.

First reported by Advanced Land Observing Satellite, Phase Array type L-band Synthetic Aperture Radar (ALOS/PALSAR) observation of night-time Amazon terrain a decade ago (Shimada et al., 2008), equatorial ionospheric scintillations have been considered as the major source of deformation in modern L-band Synthetic Aperture Radar (SAR) images (Carrano et al., 2012; Kim et al., 2017; Meyer et al., 2016). The deformation of SAR images is characterized by stripe-like structures aligned with the local geomagnetic fields, which can stretch over 1,000 km. Although a recent report shows that SAR and GPS scintillation were

observed on the same night in the Indian sector (Mohanty et al., 2018), the origin of SAR scintillation and its possible relation to EPBs are not yet observationally evident due to the lack of simultaneous observation of ionospheric density depletions.

These recent studies suggest that spaceborne SAR data can provide two-dimensional imaging of plasma density irregularities of equatorial ionosphere regardless of weather and with finer spatial resolutions than optical imaging. The objective of this paper is to report the first simultaneous observations of EPB by the ALOS-2/PALSAR-2 satellite and 630-nm airglow all-sky imager in northern Brazil in order to experimentally show what may be an origin of L-band SAR scintillation at equatorial regions in the two-dimensional form.

2. Data

The SAR images were acquired from ALOS-2/PALSAR-2 operated by the Japan Aerospace Exploration Agency (JAXA). ALOS-2 orbits at approximately 628 km in altitude at an inclination angle of 97.9° in a sun-synchronous orbit. The ALOS-2/PALSAR-2 system operates at center frequencies around 1,257.5 MHz. Each SAR image used in this study has a 70 × 70 km dimension in the azimuth (satellite track) and range (radar look) direction. The spatial resolution of the original SAR data is reduced to approximately 90 m in order to suppress the speckle effect inherent in the coherent imaging system. We analyzed seven SAR images on December 29, 2014 (ALOS-2 image ID: ALOS2032390000 - ALOS2032390060).

The all-sky imager (ASI) used in this study was installed at Boa Vista (2.49°N, 60.40°W), northern Brazil. The ASI is equipped with a 180° wide-angle fish-eye lens, a telecentric lens system, and narrow band optical filters to obtain a monochromatic image on a CCD camera. The OI 630-nm airglow emission layer extends ±50 km from the typical center altitude of 250 km.

The ASI image is transformed into a latitude/longitude coordinate with the algorithm based on Garcia et al., 1997. The transformed image has 512 × 512 pixels, and each pixel size corresponds to 2 km. One all-sky image therefore covers up to 1,024 × 1,024 km in a horizontal plane, which enables good spatial coverage of the upper atmosphere during the SAR image acquisition time. The value of hmF2 (F2-layer height of the peak electron density) derived from a local Ionosonde is 257.7 km at 04:15 UT. The time series of airglow images is provided in Figure S1.

3. Observations

Figure 1a shows the footprints of the consecutive seven SAR images acquired by ALOS-2/PALSAR-2 between 04:15:46 UT and 04:16:59 UT over the Boa Vista region on December 29, 2014. A close-up of a SAR image (image id: ALOS2032390000) is shown in Figure 1b (center location at 0.758°N/60.48°W). In Figure 1b, faint stripe-shaped patterns aligned in the northwest-southeast direction are found over the SAR backscatter power from the ground terrain features (e.g., dark structures). The observed stripe-shaped image distortions are thought to be the result of diffraction of the SAR signals due to the density irregularities along magnetic field lines on the signal propagation path in the ionosphere.

The standard SAR imaging process uses the whole azimuth bandwidth to get the highest azimuth resolution, and in this study, this image is called the full-band image. By now it is known that the reduction of the azimuth bandwidth enhances the contrast of the stripe pattern at the cost of losing azimuth resolution (Kim et al., 2017). In sub-band images, it is able to capture ionospheric propagation effects due to density irregularities in the SAR signal (Kim et al., 2017; Sato et al., 2018). Figure 1c shows the sub-band power image corresponding to 1/16th of the total bandwidth. The sub-band power image clearly shows the orientation of the scintillation stripes while the full-power image has reduced the sharpness of the stripes. From the ratio of sub- and full-power, we can extract the scintillation stripes from the background features (Figure 1d). We use the normalized sub-band power ratio for the comparison with the simultaneous observation of the ground ASI data in the rest of this article.

Figure 2a compares the airglow depletion observed by the all-sky imager at 04:16 UT and the SAR imaging area over Boa Vista. The airglow intensity depletion regions represented by dark band-like structures are

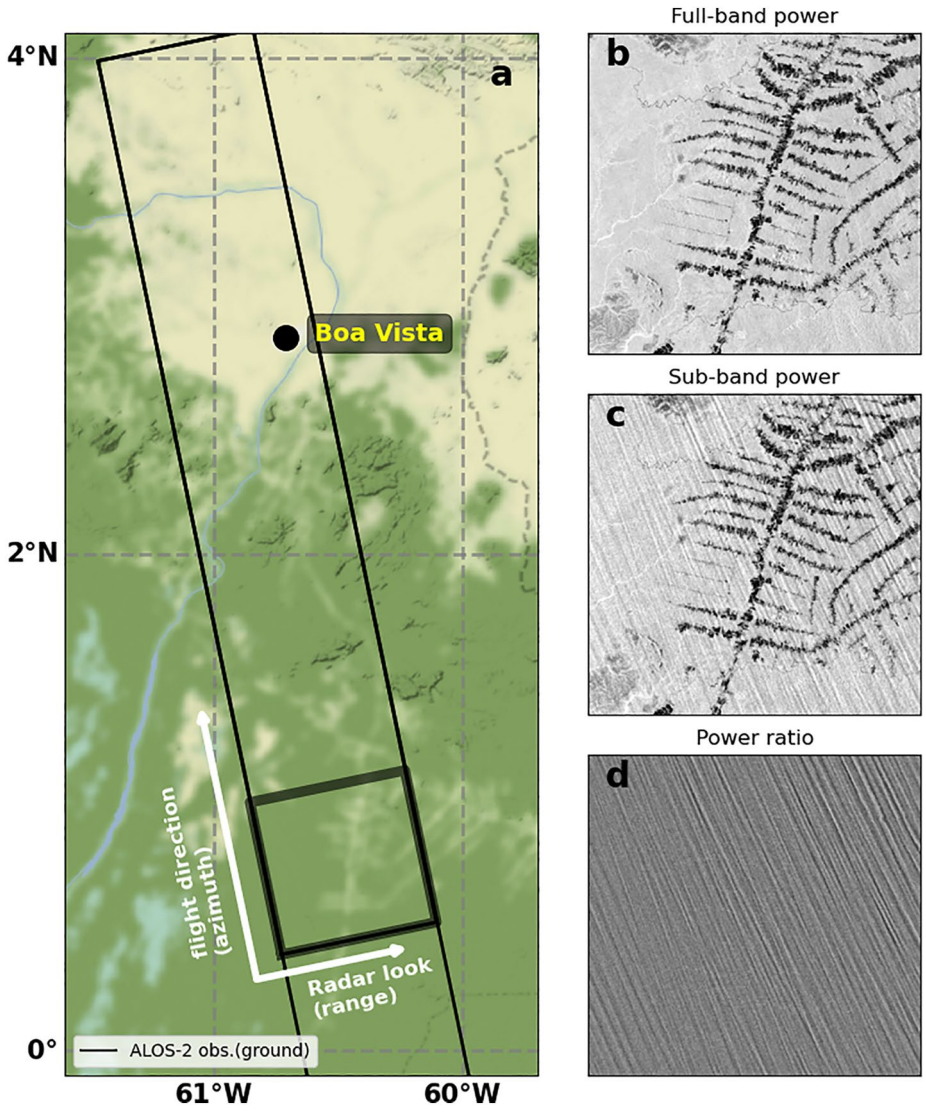

Figure 1. (a) The Advanced Land Observing Satellite-2, Phase Array type L-band Synthetic Aperture Radar-2 (ALOS-2/PALSAR-2) observation area on the terrain map near Boa Vista between 04:15:46 and 04:16:59 UT on December 29, 2014 is shown by the thin black rectangle. The SAR image containing scintillation stripes from the area denoted by the thick black rectangle (image center: 0.758°N/60.48°W) is shown in the (b) full-band power image, (c) sub-band power image from 1/16th of the azimuth spectra, and (d) the ratio of sub-band power normalized to full-band power.

the signature of plasma bubbles extending in the south-north direction at the projected altitude of 250 km. There are multiple density depletions found in the airglow image. This paper focuses on the density depletion that the SAR signals penetrate (marked by the white arrow). The SAR observation area from Figure 1a is overlaid at ground geometry (yellow dashed rectangle). The ionospheric effects on SAR images is thought to be originated from the electron concentration in the F-region that SAR radio waves penetrate at a slant in the direction between the satellite and ground. In order to indicate the topside and bottomside of the ionospheric volume that the SAR radio waves intersect, the SAR observation area is mapped on to a 300 km (dotted yellow rectangle) and 200 km altitude (solid yellow rectangle). The solid yellow rectangle has the dimension of approximately 49 × 407 km. An enlarged version of the yellow solid rectangle is also shown next to the map with purple grid lines. The band-like airglow depletion is observed to be diagonally crossing the SAR observation area slightly northward from the image center. The black arrow in Figure 2a indicates the magnetic field direction from the International Geomagnetic Reference Field (IGRF)-13 model mapped on to a 250 km altitude horizontal plane along the SAR propagation direction.

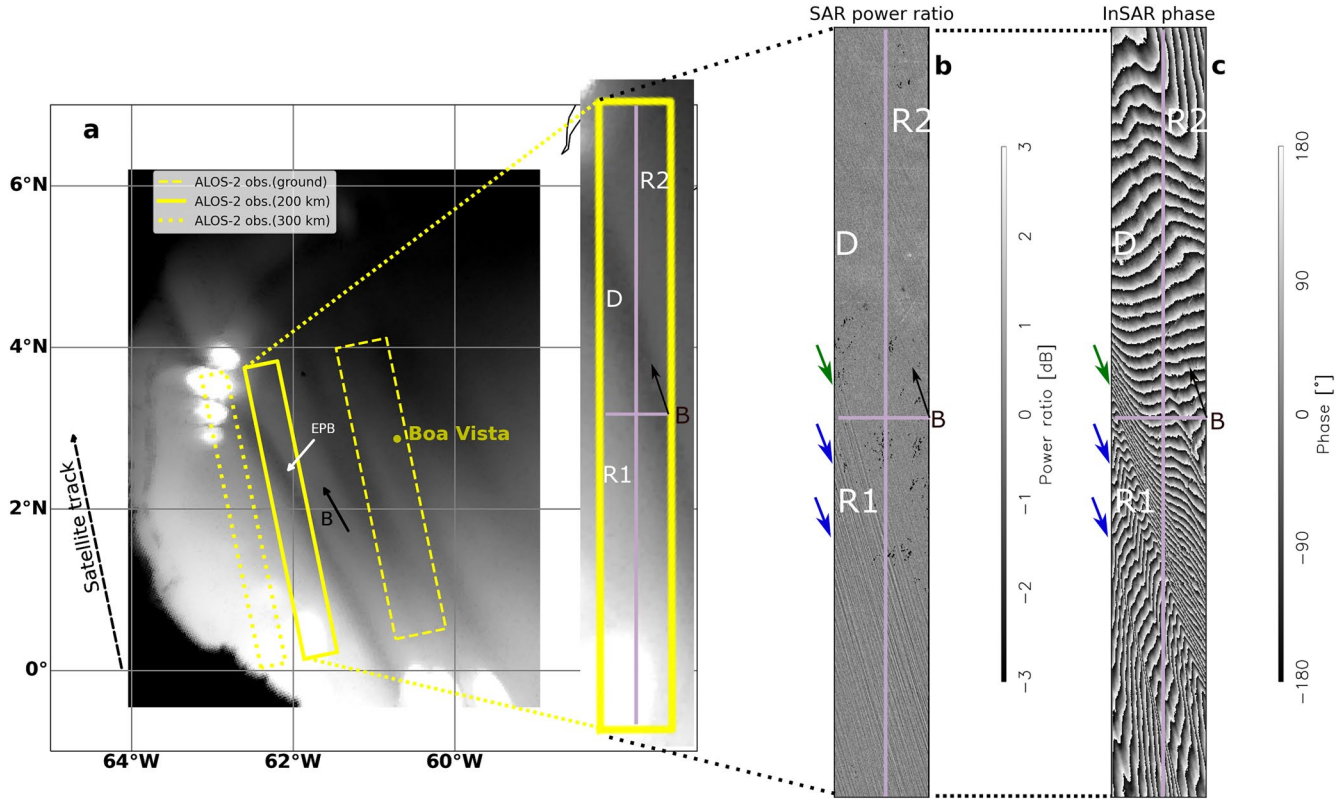

Figure 2. (a) 630-nm emission airglow image at Boa Vista at 04:16 UT on December 29, 2014. The dashed yellow rectangle shows the Advanced Land Observing Satellite-2 (ALOS-2) ground observation area from Figure 1a. The solid yellow rectangle and dotted yellow rectangle show the ALOS-2 observation area mapped onto a 200- and 300- km altitude, respectively. The plasma bubble that Synthetic Aperture Radar (SAR) signals penetrate is marked by the white arrow. The foot point of satellite track is shown by the dotted black arrow. The solid black arrows (marked by the letter B) show the magnetic field direction mapped onto a horizontal plane along SAR propagation direction. An enlarged version of the airglow in the yellow solid rectangle is shown next to the map. (b) Power ratio of the ALOS-2 SAR image showing scintillation stripe patterns. (c) SAR interferogram showing sharp phase changes near the scintillation stripes. The letter D indicates the location of airglow depletions of each image. The green arrow indicates the border location of strong scintillation stripes region (R1) in SAR power ratio, which corresponds to the location of largest SAR phase changes (the sharpest density gradients) in InSAR image. The blue arrows indicate the locations of other large SAR phase changes. The region R2 is characterized by weaker stripes and slower phase changes than R1 (see text).

Figure 2b shows the seven consecutive SAR images represented at the SAR full-/sub-power ratio. The black arrow shows the direction of the magnetic field as in Figure 1a. The stripe structures are seen most significantly on the southwest (marked by R1) of the airglow density depletion (marked by D) and somewhat weakly to the northeast (marked by R2) of the airglow depletion region. The alignment of stripe and magnetic field direction indicates that the plasma irregularities along the magnetic field that SAR signals penetrate are the source of SAR scintillation stripes. The stripe structures are very weak or indiscernible inside the depletion region. This suggests that the observed SAR scintillations are caused by plasma density irregularities primarily near the walls of the observed EPB.

In addition to SAR amplitude data, we analyzed the phase information acquired by means of the interferometric SAR (InSAR) technique. The phase differences from two SAR images contain information of horizontal TEC variations, assuming there are no other causes such as surface deformation, differences in the tropospheric delay, or a Digital Elevation Model (DEM) error (Furuya et al., 2017; Maeda et al., 2016; Pi et al., 2011). Figure 2c shows InSAR images where the interferogram consists of the image acquisitions from December 29, 2014 and from February 23, 2015 (56-day temporal baseline and normal baseline: 273.94 m).

Structured rapid phase changes are observed in the InSAR image. The region of the most rapid phase changes of SAR signal phases is observed at and to the west of the mapped location of the airglow density depletion (region R1). The maximum values of more than 50 cycles of interferometric phase changes, which correspond to a difference of approximately 25 TECU (1 TECU = 10^{16} [electrons/m^2]), are found in the

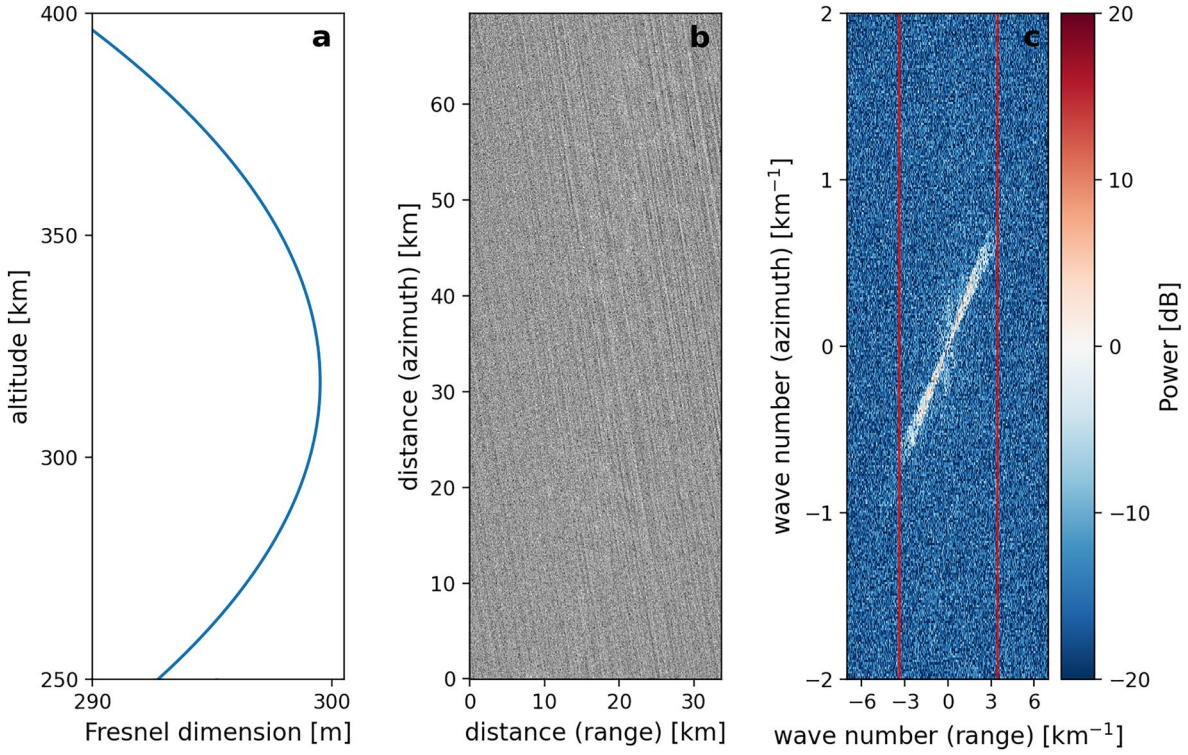

Figure 3. (a) Altitude variation of Fresnel dimension in F region for the Advanced Land Observing Satellite-2 (ALOS-2) observation on December 29, 2014. (b) Mapped Synthetic Aperture Radar (SAR) sub-band image (shown in Figure 1d) on to a 250-km altitude. (c) Two-dimensional Fourier transform of the mapped SAR sub-band image showing spatial structure of the scintillation stripes in wave numbers. The vertical red lines indicate the locations of the Fresnel dimension.

region R1. This large SAR-derived density gradient is marked by the green arrow and is located at the southwest of the airglow density depletion region. Such scales of density gradients have been previously observed by a TEC mapping technique in larger scales, which are located slightly westward from the optically observed density depletion in the Brazilian sector (Takahashi et al., 2015). Sharp SAR phase changes are also observed in the south direction from the airglow depletion (blue arrows in Figure 2c). The location of green and blue arrows corresponds to the large scintillation stripes in region R1 in Figure 2b. The SAR phase changes in the region R2 are found to be slower than in the region R1. The SAR phase changes are least varying in the region between the regions R1 and R2. The airglow and InSAR images show that the airglow density depletion region is surrounded by sharp density gradients, which coincide with the SAR scintillation stripes on December 29, 2014.

4. Discussion

The simultaneous observation of ALOS-2 and the airglow imager show that SAR scintillation stripes occurred in the vicinity of the density depletion region in the F-region ionosphere. Steep density gradients near the airglow depletion are also observed as the large interferometric phase changes in the InSAR analysis. The results suggest that plasma irregularities associated with EPBs are the source of SAR scintillation stripes. GPS observation shows that scintillation patches occurred at strong density gradient regions of the depletion, which appeared to be more intense at the western wall of the EPBs (Moraes et al., 2017). Similar phenomena have been reported for the observation of lower frequency satellite signals (Ram et al., 2012). In the observed SAR scintillation stripe power ratio image (Figure 2b), finer and stronger stripes are indeed found at the western side of the airglow density depletion. The InSAR image (Figure 3c) shows that the horizontal TEC variations become steeper from both walls toward the airglow depletion region. The area of the sharpest InSAR phase changes appears to separate the scintillation stripe region around the airglow depletion region.

The geometry of SAR observation in Figure 2 indicates that the scintillation sources exist in the F-region plasma above 200 km altitude. It should be noted that the black arrow in Figure 2 is the projection of magnetic field on a horizontal plane along SAR propagation direction, which points westwards from IGRF horizontal magnetic field. The alignment of airglow depletion with the black arrow indicates that the plasma bubble may be tilted westwards. Kil et al., 2009 explained such tilting as the shell structure of density depletion resulting from shear in the zonal plasma flow. If the plasma bubble is tilted westward, the SAR signals propagate along the west wall of plasma depletion from the topside F region through the airglow depletion height. This view agrees with the fact that the SAR scintillation stripe and steeper SAR-derived density gradients are found at the southwest of the airglow depletion region. The westwards titling of the EPB can also explain that the mapped airglow depletion is more centered around the SAR image at the bottomside than the topside of F region. As we present the first comparison of airglow and SAR observation, future observation with different satellite geometry may be able to address the location of plasma irregularities that cause SAR scintillation. VHF radar measurements show that the field-aligned irregularities occur within the entire region of EPBs (Otsuka et al., 2004).

The typical scale size of density irregularities that generate ionospheric scintillation of L-band satellite signal is given by the Fresnel dimension of the radio wave (e.g., Kintner et al., 2007). An earlier study by Carrano et al., 2012 used a phase screen model to simulate the impact of small-scale density irregularities on the ALOS/PALSAR image and suggested that the scintillation stripes could be caused by bottomside sinusoidal irregularities rather than EPBs. Here, we consider the Fresnel dimension of the observation geometry with regard to the wavelength of the SAR scintillation stripe patterns in the full-/sub-power ratio. Fresnel dimension d_f is given as $d_f = \sqrt{2\lambda\, d_1 d_2 \,/\left(d_1 + d_2\right)}$, where λ is the radio wavelength, $d_1$is the distance between the satellite and irregularity layer, and d_2 is the distance between the irregularity layer and the ground. Note that unlike the Fresnel dimensions for GPS scintillation (e.g., Kintner et al., 2007), the satellite altitude term d_1 is not negligible here. For the ALOS-2 observation on December 29, 2014, d_f is around 290–300 m in the F-region altitudes. The altitude variation of Fresnel dimension is shown in Figure 3a. We now analyze the typical scales of scintillation stripe patterns on a sub-band SAR image. Figures 3b and 3c show the sub-band SAR image of Figure 1d mapped onto a 250- km altitude and its power spectrum. Note that the distance in the range direction is shortened when mapped onto an ionospheric altitude. In Figure 3c, the wave number k and the wavelength $\lambda = k^{-1}$ of the stripe patterns are calculated for the distance in the range (horizontal) and azimuth (vertical) directions of the image. Figure 3 shows that the smallest separations of the scintillation stripe patterns (largest distance from the origin in the figure) are near the Fresnel dimension at ionospheric altitudes around the airglow depletion. Our observations therefore provide strong evidence that the Fresnel scale density irregularities in the EPBs are the primary source for the observed L-band SAR scintillation stripes.

The typical drift velocity of F-region density depletion and irregularities that scatter GPS signals are on the scale of 100 meters per second (e.g., Kriegel et al., 2017; Takahashi et al., 2015). The synthetic aperture time of the full-band image for this observation is around 1.6 s, which corresponds to 0.1 s for the 1/16th sub-band image. A 10- m drift during the sub-aperture synthesis is much smaller than the reduced resolution adopted in this study (∼90 m). The observed scintillation stripes based on sub-band power, therefore, represent snapshots of the electron density irregularities in the equatorial ionosphere.

Finally, we briefly discuss the relationship between the development of EPBs and SAR scintillation occurrence. Early studies show that EPBs contain different scale sizes of density irregularities ranging from centimeters to kilometers, among which the larger scale irregularity (0.1–1 km) can be retained to exist after the growing stage of EPBs (Basu et al., 1978). As the occurrence of equatorial ionospheric irregularities has been reported to be maximized before midnight (e.g., Kil & Heelis, 1998; Su et al., 2006), the plasma density irregularities with scale size of approximately 300 m, which cause L-band scintillation, can survive until midnight. The observational season (December in South America) and solar activity condition (near solar maximum) also favor the development of plasma bubbles at postsunset. Thus, it can be assumed that the L-band SAR scintillation stripes are caused by the plasma irregularities associated with developed EPBs where hundreds of meter scale irregularities can be still persistent.

5. Conclusions

We observed L-band SAR scintillation images simultaneously with a 630.0-nm all-sky imager in northern Brazil on December 29, 2014. The SAR scintillation stripes are aligned with the direction of a geomagnetic field that SAR signals penetrate and appeared around the density depletion region observed by the airglow emission. Stronger stripes are found at the locations of steep SAR-derived density gradients. The scintillation stripes in a SAR sub-band image have a scale size close to the Fresnel dimension of the observation geometry. The results provide observational evidence that the L-band SAR scintillation stripes, which have been discussed over the last decade, originated from the plasma density irregularities with the scale size of hundreds of meters near the density depletion region of EPBs. It is suggested that the SAR scintillation can be observed when the satellite radar signals intersect developed plasma bubbles. This study demonstrated that SAR observation provides high-resolution two-dimensional imaging of plasma density irregularities in equatorial ionosphere, which will be a useful tool to study EPBs.

Data Availability Statement

All image data and relevant parameters used within the publication are available from an online repository (https://zenodo.org/record/5121968).

Acknowledgments
ALOS-2 PALSAR-2 Level 1.1 data are provided by the Japan Aerospace Exploration Agency (JAXA) within the framework of the Earth Observation Research Announcement. The authors thank the ISEE International Collaborative Research Programs from Nagoya University. C. M. Wrasse acknowledges the support from CNPq (314972/2020-0). E. R. de Paula and J. R. Souza thank the respective support from CNPq 202531/2019-0 and 307181/2018-9 as well as the INCT GNSS-NavAer grants 2014/465648/2014-2 CNPq and 2017/50115-0 FAPESP. Open access funding enabled and organized by Projekt DEAL.

References

Basu, S., Basu, S., Aarons, J., McClure, J. P., & Cousins, M. D. (1978). On the coexistence of kilometer- and meter-scale irregularities in the nighttime equatorial F region. *Journal of Geophysical Research*, *83*(A9), 4219–4226. https://doi.org/10.1029/JA083iA09p04219

Carrano, C. S., Groves, K. M., & Caton, R. G. (2012). Simulating the impacts of ionospheric scintillation on L band SAR image formation: Scintillation impacts on SAR imagery. *Radio Science*, *47*(4). https://doi.org/10.1029/2011RS004956

Furuya, M., Suzuki, T., Maeda, J., & Heki, K. (2017). Midlatitude sporadic-E episodes viewed by L-band split-spectrum InSAR. *Earth Planets and Space*, *69*(1), 175. https://doi.org/10.1186/s40623-017-0764-6

Garcia, F. J., Taylor, M. J., & Kelley, M. C. (1997). Two-dimensional spectral analysis of mesospheric airglow image data. *Applied Optics*, *36*(29), 7374. https://doi.org/10.1364/AO.36.007374

Kil, H., & Heelis, R. A. (1998). Equatorial density irregularity structures at intermediate scales and their temporal evolution. *Journal of Geophysical Research*, *103*(A3), 3969–3981. https://doi.org/10.1029/97JA03344

Kil, H., Heelis, R. A., Paxton, L. J., & Oh, S.-J. (2009). Formation of a plasma depletion shell in the equatorial ionosphere. *Journal of Geophysical Research*, *114*(A11). https://doi.org/10.1029/2009JA014369

Kim, J. S., Papathanassiou, K. P., Sato, H., & Quegan, S. (2017). Detection and estimation of equatorial spread F scintillations using synthetic aperture radar. *IEEE Transactions on Geoscience and Remote Sensing*, *55*(12), 6713–6725. https://doi.org/10.1109/TGRS.2017.2731943

Kintner, P. M., Ledvina, B. M., & de Paula, E. R. (2007). GPS and ionospheric scintillations. *Space Weather*, *5*(9). https://doi.org/10.1029/2006SW000260

Kriegel, M., Jakowski, N., Berdermann, J., Sato, H., & Mersha, M. W. (2017). Scintillation measurements at Bahir Dar during the high solar activity phase of solar cycle 24. *Annales Geophysicae*, *35*(1), 97–106. https://doi.org/10.5194/angeo-35-97-2017

Maeda, J., Suzuki, T., Furuya, M., & Heki, K. (2016). Imaging the midlatitude sporadic *E* plasma patches with a coordinated observation of spaceborne InSAR and GPS total electron content: Imaging the midlatitude E_S with InSAR. *Geophysical Research Letters*, *43*(4), 1419–1425. https://doi.org/10.1002/2015GL067585

McNamara, L. F., Caton, R. G., Parris, R. T., Pedersen, T. R., Thompson, D. C., Wiens, K. C., & Groves, K. M. (2013). Signatures of equatorial plasma bubbles in VHF satellite scintillations and equatorial ionograms. *Radio Science*, *48*(2), 89–101. https://doi.org/10.1002/rds.20025

Meyer, F. J., Chotoo, K., Chotoo, S. D., Huxtable, B. D., & Carrano, C. S. (2016). The influence of equatorial scintillation on L-band SAR image quality and phase. *IEEE Transactions on Geoscience and Remote Sensing*, *54*(2), 869–880. https://doi.org/10.1109/TGRS.2015.2468573

Mohanty, S., Singh, G., Carrano, C. S., & Sripathi, S. (2018). Ionospheric scintillation observation using space-borne synthetic aperture radar data. *Radio Science*, *53*(10), 1187–1202. https://doi.org/10.1029/2017RS006424

Moraes, A., Costa, E., Abdu, M. A., Rodrigues, F. S., de Paula, E. R., Oliveira, K., & Perrella, W. J. (2017). The variability of low-latitude ionospheric amplitude and phase scintillation detected by a triple-frequency GPS receiver. *Radio Science*, *52*(4), 439–460. https://doi.org/10.1002/2016RS006165

Otsuka, Y., Shiokawa, K., Ogawa, T., & Wilkinson, P. (2002). Geomagnetic conjugate observations of equatorial airglow depletions: Conjugate observations of airglow depletions. *Geophysical Research Letters*, *29*(15). https://doi.org/10.1029/2002GL015347

Otsuka, Y., Shiokawa, K., Ogawa, T., Yokoyama, T., Yamamoto, M., & Fukao, S. (2004). Spatial relationship of equatorial plasma bubbles and field-aligned irregularities observed with an all-sky airglow imager and the Equatorial Atmosphere Radar. *Geophysical Research Letters*, *31*(20). https://doi.org/10.1029/2004GL020869

Pi, X., Freeman, A., Chapman, B., Rosen, P., & Li, Z., (2011). Imaging ionospheric inhomogeneities using spaceborne synthetic aperture radar: Imaging the ionosphere using SAR. *Journal of Geophysical Research*, *116*. https://doi.org/10.1029/2010JA016267

Ram, S. T., Yamamoto, M., Tsunoda, R. T., Thampi, S. V., & Gurubaran, S. (2012). On the application of differential phase measurements to study the zonal large scale wave structure (LSWS) in the ionospheric electron content. *Radio Science*, *47*(2). https://doi.org/10.1029/2011RS004870

Saito, S., Maruyama, T., Ishii, M., Kubota, M., Ma, G., Chen, Y., et al. (2008). Observations of small- to large-scale ionospheric irregularities associated with plasma bubbles with a transequatorial HF propagation experiment and spaced GPS receivers. *Journal of Geophysical Research*, *113*(A12). https://doi.org/10.1029/2008JA013149

Sato, H., Kim, J. S., Jakowski, N., & Häggström, I. (2018). Imaging high-latitude plasma density irregularities resulting from particle precipitation: Spaceborne L-band SAR and EISCAT observations. *Earth Planets and Space*, *70*(1), 163. https://doi.org/10.1186/s40623-018-0934-1

Shimada, M., Muraki, Y., & Otsuka, Y. (2008). *Discovery of anoumoulous stripes over the Amazon by the PALSAR onboard ALOS satellite. IGARSS 2008 - 2008 IEEE international Geoscience and remote sensing symposium, II-387-II–390*. https://doi.org/10.1109/IGARSS.2008.4779009

Su, S.-Y., Liu, C. H., Ho, H. H., & Chao, C. K. (2006). Distribution characteristics of topside ionospheric density irregularities: Equatorial versus midlatitude regions. *Journal of Geophysical Research*, *111*(A6). https://doi.org/10.1029/2005JA011330

Takahashi, H., Wrasse, C. M., Otsuka, Y., Ivo, A., Gomes, V., Paulino, I., et al. (2015). Plasma bubble monitoring by TEC map and 630nm airglow image. *Journal of Atmospheric and Solar-Terrestrial Physics*, *130–131*, 151–158. https://doi.org/10.1016/j.jastp.2015.06.003

Tsunoda, R. T. (1980). Backscatter measurements of 11-cm equatorial spread-F irregularities. *Geophysical Research Letters*, *7*(10), 848–850. https://doi.org/10.1029/GL007i010p00848

Yokoyama, T., Shinagawa, H., & Jin, H. (2014). Nonlinear growth, bifurcation, and pinching of equatorial plasma bubble simulated by three-dimensional high-resolution bubble model. *Journal of Geophysical Research: Space Physics*, *119*(12), 10474–10482. https://doi.org/10.1002/2014JA020708